Chemical Science

ROYAL SOCIETY OF CHEMISTRY

EDGE ARTICLE

View Article Online
View Journal | View Issue

Cite this: *Chem. Sci.*, 2025, **16**, 20536

All publication charges for this article have been paid for by the Royal Society of Chemistry

Reactivity of organic photocatalysts displaying thermally activated delayed fluorescence (TADF): rationalizing unexpected differences between rates of quenching of the lowest singlet and triplet states

Federica Fina, †[ab] Caterina Bellatreccia,†[ab] Xia Wu,[c] Pier Giorgio Cozzi, [ab] Alessandro Troisi, [c] Sergei Vinogradov [de] and Paola Ceroni *[ab]

Cyanoarene chromophores exhibiting thermally activated delayed fluorescence (TADF) are increasingly used in photoredox catalysis. At high concentrations of organic substrates, which are typically employed in preparative synthesis, the primary photoinduced electron transfer (PeT) steps in the photocatalytic processes can involve both singlet (S_1) and triplet (T_1) excited states of TADF chromophores, despite very short lifetimes (nanoseconds) of the former. However, the difference between the reactivities of these states is not well understood, while being critically important for the photocatalytic process. In this work, three representative TADF chromophores were examined in reductive and oxidative PeT quenching reactions. First, using kinetic simulations, we assert that Stern–Volmer quenching plots based on the experimentally measured prompt and delayed fluorescence lifetimes, but not integrated intensities, yield accurate bimolecular rate constants for the PeT quenching reactions involving S_1 and T_1 excited states. Secondly, experimental measurements of prompt and delayed fluorescence reveal significantly higher quenching constants for reductive quenching of S_1 compared to T_1 states, while for oxidative quenching the rate constants are nearly equal. Electronic structure calculations provide insight into the difference between the PeT rates for reductive quenching, suggesting that it might stem from the different spatial hole–electron distributions in S_1 and T_1 states. Taken together, our findings bring crucial information about the photocatalytic process involving TADF chromophores that should aid the design of the next-generation of TADF photocatalysts.

Received 4th July 2025
Accepted 29th September 2025

DOI: 10.1039/d5sc04948b

rsc.li/chemical-science

Introduction

Several members of the family of organic compounds exhibiting thermally activated delayed fluorescence (TADF) are being successfully employed in photocatalysis.[1–9] The structures of the most commonly used TADF photocatalysts (PC) feature an electron-withdrawing core, commonly isophthalonitrile, surrounded by electron donor moieties, such as carbazolyl or diphenylamine units. The lowest excited electronic states of these chromophores possess distinct periphery-to-core charge transfer character, whereby upon photoexcitation the charge migrates from the peripherally located HOMO onto the core-centred LUMO. However, due to the large torsion angles between the π-systems of the core and appended donor groups, the overlap between the HOMO and LUMO is insignificant, resulting in a rather small difference between the energies of S_1 and T_1 excited states, usually lower than 0.3 eV.[10–14] Consequently, TADF chromophores exhibit a distinctive photophysical behaviour: upon photoexcitation, followed by efficient $S_1 \rightarrow T_1$ intersystem crossing (isc) and population of the T_1 state, thermally-induced reverse $T_1 \rightarrow S_1$ intersystem crossing (risc), facilitated by the small S_1–T_1 energy gap, takes place. Once a molecule transitions back to the S_1 state *via* risc, it rapidly decays to the ground state with emission of fluorescence. Thus, fluorescence in such systems typically exhibits a biexponential decay: a shorter component, usually in the range of few nanoseconds, known as *prompt* fluorescence, and a longer component in the range of microseconds, referred to as *delayed* fluorescence.

The widespread use of TADF chromophores in photocatalysis and, more specifically, in photoredox catalysis, stems from: (i) availability *via* easy synthetic procedure; (ii) tunable

[a]*Alma Mater Studiorum-Dipartimento di Chimica "G. Ciamician", Università di Bologna, Via Gobetti 83, Bologna 40129, Italy. E-mail: paola.ceroni@unibo.it*

[b]*Center for Chemical Catalysis - C3, Alma Mater Studiorum, Università di Bologna, Via Gobetti 83, Bologna 40129, Itlay*

[c]*Department of Chemistry, University of Liverpool, Liverpool L69 7ZD, UK*

[d]*Department of Biochemistry and Biophysics, Perelman School of Medicine, University of Pennsylvania, Philadelphia, USA*

[e]*Department of Chemistry, School of Arts and Sciences University of Pennsylvania, Philadelphia, USA*

† Authors contributed equally.

redox properties by modification of either the core or the acceptor units;[15] (iii) close energetic proximity of S_1 and T_1 states, so that only a small fraction of energy is lost when S_1 transitions to T_1 *via* isc, while, at high substrate concentrations, both states can participate in the photoinduced electron transfer (PeT) reactions.[16–19]

Nevertheless, despite the interest in using TADF chromophores as photocatalysts, the quenching of their S_1 and T_1 states by PeT is not well understood, while being critically important for the photocatalytic process. For example, recently we observed that reductive quenching of the prompt fluorescence of **4DPAIPN** (Fig. 1, $k_{qp} = 2.7 \times 10^9$ M^{-1} s^{-1}) by PeT from 1,3-dimethyl-2-phenyl-2,3-dihydro-1H-benzimidazole (BIH) is characterized by a more than 10-fold higher quenching constant than quenching of the delayed fluorescence ($k_{qd} = 1.5 \times 10^8$ M^{-1} s^{-1}).[20] Similarly, we observed faster quenching of S_1 compared to T_1 in the case of the quenching of another TADF chromophore, namely 9,9'-(sulfonylbis(pyrimidine-5,2-diyl)) bis(3,6-di-*tert*-butyl-9*H*carbazole) pDTCz-DPmS by four different electron donors.[21] Since the energies of the S_1 and T_1 states of **4DPAIPN** are close (*vide infra*), the driving forces (ΔG) of the PeT processes involving these states should be similar, and, therefore, one would expect only a small difference between the corresponding quenching rate constants. The objective of the present study was to understand the origin of this anomalous behaviour by analysing other isophthalonitrile-based TADF chromophores (Fig. 1) and other quenchers to determine whether the difference persists across a broader set of compounds and to rationalize the experimental findings with the help of kinetic simulations and computational analysis.

Results and discussion

Kinetic simulations

Most of the TADF chromophores discussed in the literature can be schematically described by the Jablonski diagram depicted in Fig. 2. In the absence of quencher Q, the evolution of the

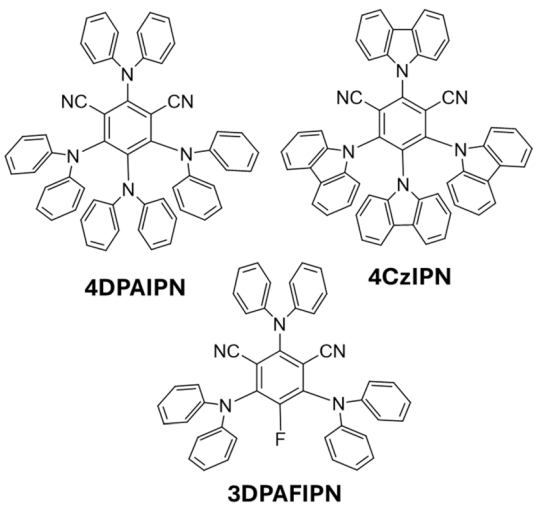

Fig. 1 Structures of the investigated TADF photocatalysts.

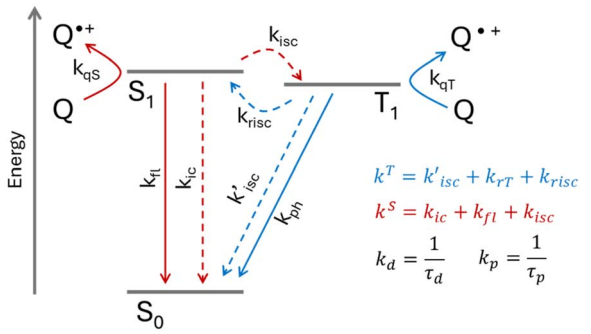

Fig. 2 Jablonski diagram of a TADF chromophore and reductive photoinduced electron transfer in the presence of quencher Q. The rate constants of fluorescence (k_{fl}), phosphorescence (k_{ph}), internal conversion (k_{ic}), inter system crossing (k_{isc} and k'_{isc}) and reverse inter system crossing (k_{risc}) and quenching processes (k_{qS} and k_{qT}) are as indicated.

populations of the lowest excited states S_1 and T_1 is described by eqn (1)–(4), which can be derived analytically:[22]

$$[S_1] = \frac{[S_1]_{t=0}}{k_p - k_d}\left[(-k^T + k_p)e^{-k_p t} + (k^T + k_d)e^{-k_d t}\right] \quad (1)$$

$$[T_1] = [S_1]_{t=0}\frac{k_{isc}}{k_p - k_d}\left[e^{-k_p t} - e^{-k_d t}\right] \quad (2)$$

$$k_p = \frac{1}{\tau_p} = \frac{1}{2}\left(k^S + k^T + \sqrt{(k^S - k^T)^2 + 4k_{risc}k_{isc}}\right) \quad (3)$$

$$k_d = \frac{1}{\tau_d} = \frac{1}{2}\left(k^S + k^T - \sqrt{(k^S - k^T)^2 + 4k_{risc}k_{isc}}\right) \quad (4)$$

where k^S and k^T are the sums of the rate constants of all the processes deactivating the S_1 and T_1 excited states, respectively; k_{isc} is the rate constant of $S_1 \rightarrow T_1$ intersystem crossing and k_{risc} is the rate constant of the reverse process; τ_p and τ_d, as defined by eqn (3) and (4), refer to the prompt and delayed emission lifetimes, respectively.

We performed kinetic simulations by numerical integration of the rate equations of a TADF system. In these simulations, a specific combination of kinetic constants of Fig. 2 (input parameters) yields simulated traces of S_1 and T_1, which can be fitted with biexponential functions to obtain τ_{1S}, τ_{2S}, τ_{1T} and τ_{2T} (output values, see SI for more details). The time constants obtained by the fitting of the simulated S_1 trace (τ_{1S}, τ_{2S}) correspond to the lifetimes obtained by fitting of the fluorescence decay in a real experiment. As expected, the simulated decay of S_1 in absence of the quencher is always in agreement with the exact solution, meaning that τ_{1S} and τ_{2S} match with τ_p, τ_d calculated *via* eqn (3) and (4) based on the input parameters (Table S1). In addition to that, our simulated data show that, under any combination of kinetic constants, the longer lifetime obtained by the fitting of S_1 trace (τ_{2S}) matches with the decay lifetime of the T_1 trace (τ_{2T}), demonstrating that the delayed fluorescence lifetime mirrors T_1 decay. The importance of this finding stems from the fact that for most common TADF organic photocatalysts $T_1 - > S_0$ phosphorescence, which would

be considered a direct signature of the T_1 state, is not observable at ambient temperatures and measuring evolution of the triplet state by transient absorption experiments[23–25] is not straightforward to set-up and/or interpret. Instead, the analysis of delayed fluorescence is simpler and more accessible from the experimental point of view.

In the presence of the quencher, it is necessary to assess how the quenching constants k_{qp} and k_{qd}, experimentally determined by prompt and delayed fluorescence quenching, can be correlated to the quenching constants of S_1 and T_1, namely k_{qS} and k_{qT}. To address this issue, we run kinetic simulations introducing the quenching terms in the differential equations of S_1 and T_1. Each rate constant shown in Fig. 2 was varied over three orders of magnitude in the simulations (see Table S1). For each combination of kinetic constants, the concentration of the quencher [Q] was varied to generate the respective [S_1] decays, which were then fitted (using the non-linear least squares method) with a bi-exponential equation:

$$[S_1] = A_1 \times e^{(-t/\tau_{1S})} + A_2 \times e^{(-t/\tau_{2S})} \quad (5)$$

The extracted values of τ_{1S} (shorter lifetime) and τ_{2S} (longer lifetime) were used to generate simulated Stern–Volmer plots, from which the respective output quenching constants k_{qp} and k_{qd} were obtained by linear fitting (Fig. 3a, b and Table S1). The performed simulations unambiguously showed that the quenching constants k_{qp} and k_{qd}, obtained by the numerical treatment described above, match the constants k_{qS} and k_{qT} that were used generate the decays (Fig. 3a, b and SI).

The key findings of our modelling, which can be translated to real experiments, are the following: (i) for any combination of rate constants and quencher concentration, the delayed lifetime of S_1, easily measurable by time-resolved fluorescence, matches with the decay lifetime of T_1; (ii) the rate constants obtained from Stern–Volmer experiments for prompt and delayed fluorescence lifetimes (k_{qp} and k_{qd}) are the quenching constants of the singlet (k_{qS}) and the triplet states (k_{qT}), respectively.

The physical meaning of these results is that when the rates of prompt and delayed fluorescence differ by three or more orders of magnitude, S_1 state does not get populated to any significant extent during the emission of delayed fluorescence, but is visited transiently, merely providing a radiative deactivation channel for the T_1 state. Thus, all chemistry involving S_1 state occurs during the initial phase right after the irradiation pulse (prompt fluorescence regime). At later times, chemical reactions are carried out almost exclusively by T_1 state, whose evolution is mirrored by delayed fluorescence. Thus, the difference between k_{qp} and k_{qd} for isophthalonitrile-based TADF molecules, which was reported earlier,[20,21] reflects the difference between the PeT quenching rate constants for the respective S_1 and T_1 states (k_{qS} and k_{qT}). Considering the importance of TADF fluorophores for the field of photocatalysis, understanding of the physical origin of this difference is crucial for the development of new optimized catalytic systems.

Notably, Stern–Volmer plots constructed using integrated intensities, as opposed to lifetimes, are highly non-linear (Fig. 3c), which is expected for biexponential decays, whose integrals do not correlate with the underlying individual rate constants. Limburgh has proposed a formula to obtain k_{qS} and k_{qT} from the fitting of the non-linear trend of intensities.[26] Nevertheless, this approach requires the evaluation of 3 parameters ($k_{isc}k_{risc}$, k_{qS} and k_{qT}) from a single set of experimental data, which leads to high uncertainty on the determined parameters. On the other hand, the Stern–Volmer analysis on emission lifetimes allows to obtain 2 parameters (k_{qS}, k_{qT}) from 2 distinct sets of data (τ_p and τ_d), ensuring higher precision in the evaluation of the quenching constants. Therefore, using emission lifetimes for determination of k_{qS} and k_{qT} should be

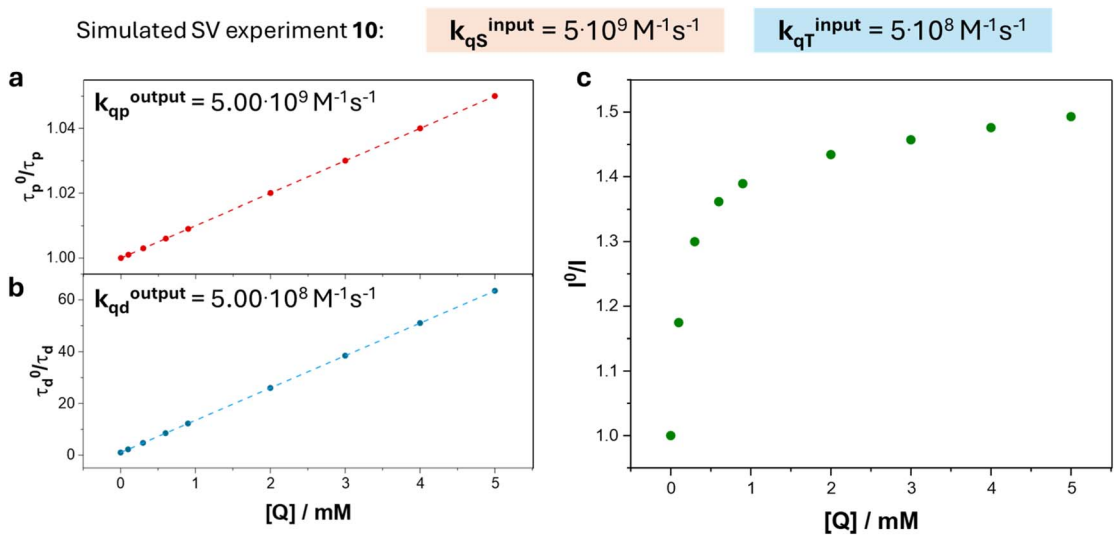

Fig. 3 Simulated Stern–Volmer plots for selected sets of parameters ($\tau^0p = 2 \times 10^{-9}$ M^{-1} s^{-1}, $\tau^0{}_d = 2.5 \times 10^{-5}$ M^{-1} s^{-1}. For further details, see Table S1, experiment 10) calculated on τ_p (a), τ_d (b) and on emission intensity (c). The data in (a) and (b) were fitted with straight lines, and the extracted quenching rate constants k_{qp} and k_{qd} matched the input constants k_{qS} and k_{qT} used to synthesise the data with high accuracy (see Table S2 for all the fitting parameters).

preferred over using integrated intensities. Unfortunately, in the majority of the literature reports on TADF chromophores in photoredox catalysis, Stern–Volmer analyses have been carried out using linear fitting of luminescence intensities, and, therefore, the extracted quenching constants are inaccurate.

Quenching experiments

Stern–Volmer quenching experiments, utilizing either prompt or delayed fluorescence lifetimes, were performed for three well-known TADF photocatalysts, **4DPAIPN**, **4CzIPN**, and **3DPAFIPN** (Fig. 1), with *N*,*N*-diisopropylethylamine (DIPEA), a commonly used sacrificial electron donor,[27] as a quencher. The measurements were carried out in toluene solutions. Reductive PeT quenching follows the equation:

$$*\mathrm{TADF} + \mathrm{Q} \rightarrow \mathrm{TADF}^{\bullet-} + \mathrm{Q}^{\bullet+} \quad (6)$$

where *TADF is either S_1 or T_1 excited state upon photoexcitation.

In the case of **4DPAIPN** and **3DPAFIPN**, the quenching constant for S_1 state, k_{qS}, extracted from the prompt fluorescence measurements, was found to be *ca.* 3 orders of magnitude higher than that for T_1 state, k_{qT}, obtained using delayed fluorescence. For **4CzIPN**, k_{qS} was 3 times higher than k_{qT} (Table 1). To rationalise these results, we calculated the free energies (ΔG) for the PeT processes (6) involving S_1 and T_1 states using the ground-state redox potentials, measured in dichloromethane (DCM), and the spectroscopic energy E_{00} estimated from the fluorescence and phosphorescence spectra registered at 77 K (see Fig. S2–S5):

$$\Delta G = F[E(\mathrm{TADF/TADF}^{\bullet-}) - E(\mathrm{Q}^{\bullet+}/\mathrm{Q})] + E_{00}(\mathrm{TADF/*TADF}) \quad (7)$$

It is worth noting that the analysed TADF chromophores in dichloromethane solution display a chemically and electrochemically reversible electron transfer process in the cathodic region (Fig. S6), while DIPEA is reported to undergo chemically irreversible electron transfer process in the anodic region and significantly different redox potentials are reported in the literature also in the same solvent.[28–30] We assumed a value of $E(\mathrm{DIPEA}^{\bullet+}/\mathrm{DIPEA}) = 0.94$ V *vs.* SCE, based on one of the literature reports,[28] but uncertainty of this value is reflected in the calculated ΔG.

As expected, when the PeT driving force was positive, like in the case of case of T_1 state of **4DPAIPN**, the quenching constant (k_{qT}) was small. However, the driving force is clearly not the only factor that defines the difference between the quenching rate constants for the studied PeT reactions. For example, the ΔG values for the processes involving S_1 of **4DPAIPN** and T_1 of **3DPAFIPN**, are very similar, while the respective quenching constants are different by 3 orders of magnitude.

To eliminate the uncertainty in the ΔG values stemming from the irreversibility of DIPEA oxidation, the measurements were carried out using ferrocene derivatives as electron donors (Fig. 4) that, in contrast to DIPEA, display a chemically reversible anodic electron transfer process (Fig. S7) with redox potentials such that the PeT processes involving either S_1 or T_1 states of all of the studied TADF sensitizers are exergonic. The absorption spectra of the photosensitizers and ferrocene-based quenchers correspond to the sum of the spectra of the isolated compounds (see Fig. S14), and both prompt and delayed fluorescence decays can be individually fitted with a mono-exponential function (Fig. S15–S24). Therefore, there is no evidence of static quenching and the kinetic constants determined are solely attributed to dynamic quenching. The measured quenching constants were found to be in the range of 10^8–10^{10} M^{-1} s^{-1}, and the quenching constants for S_1 were consistently higher than for T_1 (Table 2).

It should be noted that the same trend is also observed in DCM (Fig. S15 and S18), suggesting that the polarity of the solvent does not significantly affect the quenching dynamics.

As expected, the differences became smaller and eventually vanished (for example, see the data for **4CzIPN** and FcCHO quencher) as the constants approached the diffusion limit, taken as an approximation as the self-diffusion of toluene (k_d =

Table 1 One-electron reduction potential (in V *vs.* SCE) of the photocatalysts (PC) in dichloromethane (DCM), excitation energies corresponding to their S_1 and T_1 states, PeT (6) free energy (ΔG) and the corresponding quenching constants (k_q) measured in air-equilibrated (for S_1 quenching) and deaerated (for T_1 quenching) toluene solutions

PC	E/V *vs.* SCE	E_{00}/eV		ΔG^a/eV	k_q/M^{-1} s^{-1}
4DPAIPN	−1.67	S_1	0.94	0.00	1.3×10^8
		T_1	0.78	0.16	7.4×10^4
4CzIPN	−1.25	S_1	1.64	−0.70	5.6×10^9
		T_1	1.56	−0.62	2.9×10^9
3DPAFIPN	−1.63	S_1	1.22	−0.28	3.6×10^8
		T_1	0.97	−0.03	2.2×10^5

[a] ΔG is calculated assuming $E(\mathrm{DIPEA}^{\bullet+}/\mathrm{DIPEA}) = 0.94$ V *vs.* SCE.[28]

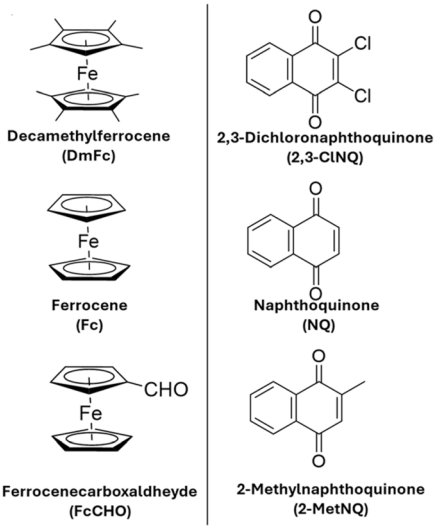

Fig. 4 Structures of (a) ferrocene derivatives (electron donors) and (b) naphthoquinone derivatives (electron acceptors) used as quenchers in PET reactions.

Table 2 Redox potentials (in V *vs.* SCE) of the quenchers in DCM, PeT (8) free energy (ΔG) and the corresponding quenching constants (k_q) measured in air equilibrated (for S_1 quenching) and deaerated (for T_1 quenching) toluene solutions

Photocatalyst	Quencher	E/V *vs.* SCE	State	ΔG/eV	$k_q/10^9$ M^{-1} s^{-1}
4DPAIPN	Fc	0.39	S_1	−0.48	9.4
			T_1	−0.32	2.0
	FcCHO	−0.16	S_1	−0.18	8.5
			T_1	−0.02	1.5
	DmFc	0.69	S_1	−1.03	12
			T_1	−0.87	9.0
4CzIPN	Fc	0.39	S_1	−1.18	14
			T_1	−1.10	11
	FcCHO	−0.16	S_1	−0.88	15
			T_1	−0.79	15
	DmFc	0.69	S_1	−1.73	7.9
			T_1	−1.65	2.2
3DPAFIPN	Fc	0.39	S_1	−0.77	3.5
			T_1	−0.51	0.81
	FcCHO	−0.16	S_1	−0.46	10
			T_1	−0.20	3.8
	DmFc	0.69	S_1	−1.31	4.5
			T_1	−1.05	1.0

1.2×10^{10} M^{-1} s^{-1}).[31] The Rehm–Weller plot (Fig. S28), constructed assuming the same electronic and nuclear factors (ν_N, κ_{el}, λ, see SI for more details) for the PC/Q couples in Table 2 did not reveal any correlation between the quenching rates and the PeT driving forces (ΔG) in the series. Therefore, the difference between the quenching constants for S_1 and T_1 states of the same photocatalyst cannot be explained solely on the basis of ΔG of the respective reactions, *i.e.* S_1 state being a stronger oxidant than T_1 state.

It is important to mention that while the cage escape of the geminate radical pair $TADF^{\bullet-}\ldots Q^{\bullet+}$ and radical-pair recombination are important for the outcome of the overall catalytic cycle,[32,33] spin selectivity on these processes do not influence the rates of the PeT reactions, since they occur after the quenching process.

Next, we examined oxidative PeT reactions involving one of the TADF chromophores, **4CzIPN**. Such reactions follow the equation:

$$^*TADF + Q \rightarrow TADF^{\bullet+} + Q^{\bullet-} \quad (8)$$

Three naphthoquinone derivatives (Fig. 4) were selected as quenchers based on the established chemical reversibility of their cathodic electron transfer process and considering the exergonicity of processes (8) involving either S_1 or T_1 states of **4CzIPN**.

Remarkably, unlike in the case of reductive quenching, the values of k_{qS} and k_{qT} (Table 3) for reactions with naphthoquinones were found to be very similar (<10% difference, Fig. 5 and Table 3).

Computational study

A possible explanation of the experimental observations is that the electron transfer couplings are larger for S_1 than for T_1 in the case of reductive quenching, while they are approximately the same for oxidative quenching. We have therefore performed electronic structure TDDFT calculations for **4CzIPN**, **4DPAIPN**, and **3DPAFIPN** in toluene (as in the measurements) modelled as a continuum dielectric. The results are similar to analogous calculations presented in literature[35] (the computational details are given in the SI) with a slightly overestimated gap between T_1 and S_1 common for TADF molecules[36] and the lowest transition having the character of an intramolecular charge transfer from the core of the molecule to the external shell.

The key new analysis to explain the observations in this paper is the hole and electron distributions in the adiabatic S_1 and T_1 states presented in Fig. 6, with a visual decomposition of the molecule into "core" (orange) and "shell" (green) fragments. For all three TADF chromophores there is a highly relevant change between the location of the hole density in S_1 and T_1. The hole density is much larger in the core fragment for T_1 (32–48%) with respect to S_1 (4–16%) and, as a consequence, we expect a reduced rate to accept an electron in T_1 *via* reductive quenching because the core fragment is not in contact with the quencher. Conversely, the electron density is fairly similar between T_1 and S_1 across the three molecules consistent with

Table 3 Redox potentials (in V *vs.* SCE) of the quenchers in Dichloromethane, free energy difference (ΔG) of the photoinduced electron transfer (4) and the related quenching constants (k_q) measured in air equilibrated (for S_1 quenching) and deaerated (for T_1 quenching) toluene solution

PC	Q	E^a/V *vs.* SCE	ΔG^b/eV		$k_q/10^9$ M^{-1} s^{-1}
4CzIPN	2,3-ClNQ	−0.38	S_1	−1.31	4.7
			T_1	−1.05	4.5
	NQ	−0.69	S_1	−0.77	5.6
			T_1	−0.51	5.0
	2-MetNQ	−0.73	S_1	−0.46	3.7
			T_1	−0.20	3.5

[a] Redox potentials of the quinone derivatives in dichloromethane.[34] [b] ΔG is calculated by considering $E(\mathbf{4CzIPN}^{\bullet+}/\mathbf{4CzIPN}) = 1.52$ V *vs.* SCE.[27]

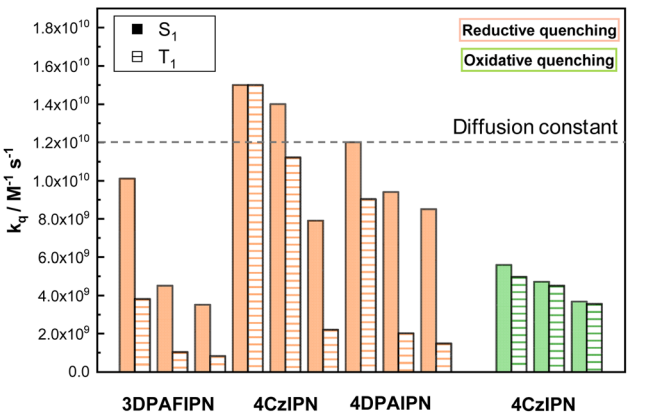

Fig. 5 Rate constants of reductive and oxidative quenching processes involving S_1 and T_1 states of selected TADF chromophores measured in toluene solution (values reported in Tables 2 and 3).

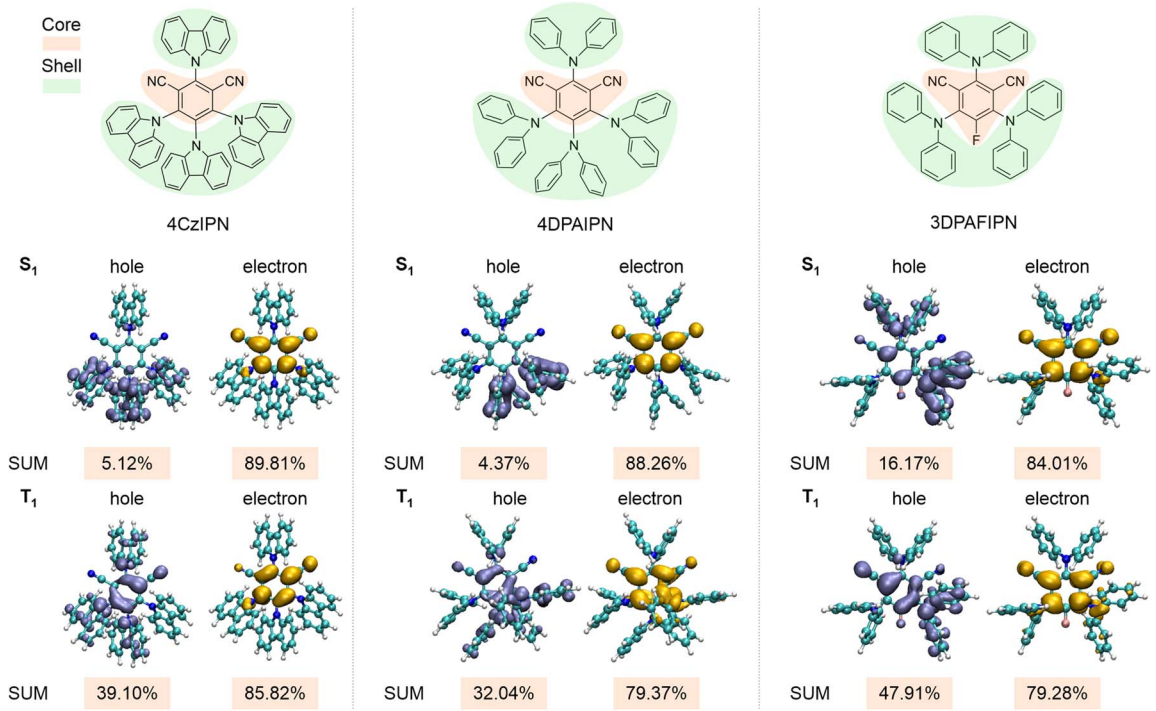

Fig. 6 Computed electron and hole density distributions in adiabatic S_1 and T_1 states for **4CzIPN**, **4DPAIPN**, and **3DPAFIPN**. SUM refers to total density of hole or electron in the core fragment.

a similar rate of oxidative quenching for singlet and triplet. It should be noted that this situation is relatively uncommon as simpler chromophores often have the lowest singlet and triplet excited states sharing a similar HOMO–LUMO configuration, with almost identical hole and electron density. On the other hand, in this case, different combinations of intramolecular charge transfer transitions are involved in S_1 and T_1. This observation is robust not only across the three molecules considered but it is also not sensitive to changes in the solvent model and is seen also in vertical rather than adiabatic transitions (see SI for further detail).

Conclusion

TADF chromophores based on an isophthalonitrile core with appended electron donating groups are widely employed in photoredox catalysis. The first step of the photocatalytic cycle is quenching of a photocatalyst excited state. Previous reports have shown the possibility of the involvement of both the lowest singlet and triplet excited states in the quenching process.[19] However, the detailed kinetic analysis of these quenching processes has not been performed before. Here, we performed a detailed kinetic study of photoinduced reductive and oxidative electron transfer processes involving S_1 and T_1 states of three representative TADF chromophores in the presence of electron donor and electron acceptor quencher molecules.

The key findings of the present study are as follows: (i) the decay of the delayed fluorescence in TADF fluorophores mirrors the dynamics of T_1 state, so that the kinetics of T_1 state can be measured using fluorescence spectroscopy rather than transient absorption methods; (ii) Stern Volmer plots based on the prompt and delayed fluorescence lifetimes yield the quenching rate constants for the reactions of S_1 and T_1 states, respectively; (iii) for the TADF chromophores studied, reductive quenching involving S_1 state is considerably faster compared to that involving T_1 state, while the energy difference between S_1 and T_1 do not fully account for the observed difference; (iv) electronic structure calculations suggest that the difference between the quenching rates for S_1 and T_1 states is related to the difference between the hole–electron density distributions in these states. In S_1 state the hole is more peripherally located, facilitating reactions in which the photocatalyst serves as an electron acceptor (reductive quenching).

Future studies will aim to determine whether the observed effects are present in other classes of TADF chromophores, such as Cu(I) complexes or Zn(II) porphyrins, to define the scope and limitations of the present findings. Furthermore, cage escape yields for the radical pair (*e.g.*, $TADF^{\bullet-}\ldots Q^{\bullet+}$) generated by quenching S_1 or T_1 excited states will be investigated. S_1 is generally expected to have lower cage-escape yield based on spin considerations. The initial spin state of the radical pair matches that of the original excited state (S_1 or T_1). Fast spin-allowed singlet charge recombination is expected to effectively compete with cage escape,[37,38] whereas the latter should outcompete the much slower spin-forbidden triplet charge recombination. Indeed, it has been recently demonstrated that the overall efficiency of the reaction depends critically on which excited state undergoes reductive quenching and, as expected, the triplet was found to be more productive.[38] This observation highlights the importance of promoting efficient quenching

from the triplet state while minimizing quenching from the singlet. From this perspective, the insights gained from our study are especially significant, as they clarify the underlying factors responsible for the relative difference in quenching rates for the singlet and triplet excited state. Overall, these findings integrate and complement existing strategies for the rational engineering of efficient TADF photocatalysts[15,18] by opening up new perspectives, including the design of sensitizers with hole densities in the T_1 state located at the periphery to facilitate reductive electron transfer processes, ultimately enhancing the efficiency and selectivity of the catalytic process.

Author contributions

F. F., C. B. and P. C. conceived the study, performed the photophysical analysis, prepared the manuscript and finalized the paper. S. V. provided the code and useful suggestions for the simulation and prepared the manuscript. P. G. C. provided the organic chromophores employed and prepared the manuscript. X. W. performed the computational study under the supervision of A. T. and together prepared the manuscript. All authors agreed on the submission of the final version of the paper.

Conflicts of interest

There are no conflicts to declare.

Data availability

The data that support the findings of this study are available from the corresponding author upon reasonable request.

Supplementary information is available. See DOI: **https://doi.org/10.1039/d5sc04948b**.

Acknowledgements

A. T. and X. W. acknowledge the funding from the European Union (European Innovation Council, project no. 101057564). F. F., C. B. and P.C. acknowledge the project LEAF funded by the MUR Progetti di Ricerca di Rilevante Interesse Nazionale (PRIN) Bando 2022 PNRR – grant P20229 L2EE.

References

1 M. A. Bryden and E. Zysman-Colman, *Chem. Soc. Rev.*, 2021, **50**, 7587–7680.
2 T. Y. Shang, L. H. Lu, Z. Cao, Y. Liu, W. M. He and B. Yu, *Chem. Commun.*, 2019, **55**, 5408–5419.
3 P. P. Singh and V. Srivastava, *Org. Biomol. Chem.*, 2021, **19**, 313–321.
4 F. Ni, J. Zhang, Y. Zhou and L. Qiu, *Chem Catal.*, 2024, **4**(5), 100915.
5 R. Hojo, A. M. Polgar and Z. M. Hudson, *ACS Sustainable Chem. Eng.*, 2022, **10**(30), 9665–9678.
6 M. A. Bryden, F. Millward, T. Matulaitis, D. Chen, M. Villa, A. Fermi, S. Cetin, P. Ceroni and E. Zysman-ColmanJ, *Org. Chem.*, 2023, **88**(10), 6364–6373.
7 A. D. Kharlamova, A. D. Averin, G. N. Bondarenko, A. S. Abel and I. P. Beletskaya, *Adv. Synth. Catal.*, 2025, **367**, e202400956.
8 J. Peng, A. Wang, Y. Liu, F. Chen, G. Tang and Y. Zhao, *Org. Lett.*, 2024, **26**(43), 9316–9321.
9 H. Zhang, Z. Cui, J. Wang, L. Zhu and C. Li, *Org. Chem. Front.*, 2024, **11**, 4502–4507.
10 T. J. Penfold, F. B. Dias and A. P. Monkman, *Chem. Commun.*, 2018, **54**, 3926–3935.
11 F. B. Dias, T. J. Penfold and A. P. Monkman, *Methods Appl. Fluoresc.*, 2017, **5**, 012001.
12 P. L. Santos, J. S. Ward, P. Data, A. S. Batsanov, M. R. Bryce, F. B. Dias and A. P. Monkman, *J. Mater. Chem. C*, 2016, **4**, 3815.
13 H. Noda, X.-K. Chen, H. Nakanotani, T. Hosokai, M. Miyajima, N. Notsuka, Y. Kashima, J.-L. Brédas and C. Adachi, *Nat. Mater.*, 2019, **18**, 1084–1090.
14 M. Y. Wong and E. Zysman-Colman, *Adv. Mater.*, 2017, **29**, 1605444.
15 V. K. Singh, C. Yu, S. Badgujar, Y. Kim, Y. Kwon, D. Kim, J. Lee, T. Akhter, G. Thangavel, L. S. Park, J. Lee, P. C. Nandajan, R. Wannemacher, B. Milián-Medina, L. Lüer, K. S. Kim, J. Gierschner and M. S. Kwon, *Nat. Catal.*, 2018, **1**, 794–804.
16 F. Hundemer, L. Graf von Reventlow, C. Leonhardt, M. Polamo, M. Nieger, S. M. Seifermann, A. Colsmann and S. Bräse, *Chemistry Open*, 2019, **8**, 1413–1420.
17 J. Luo and J. Zhang, *ACS Catal.*, 2016, **6**(2), 873–877.
18 E. Speckmeier, T. G. Fische and K. Zeitler, *J. Am. Chem. Soc.*, 2018, **140**, 15353–15365.
19 J. Zhang, T.-F. Xiao, H. Zhao, J. Kong, Z. Kuang, M. Zhou, G.-Q. Xu, Y. Li and A. Xia, *J. Phys. Chem. Lett.*, 2024, **15**(47), 11784–11791.
20 E. Bassan, R. Inoue, D. Gabry, F. Calogero, S. Potenti, A. Gualandi, P. G. Cozzi, K. Kamogawa, P. Ceroni, Y. Tamaki and O. Ishitani, *Sustain Energy Fuels*, 2023, **7**, 3454.
21 M. A. Bryden, M. Villa, A. Fermi, P. Ceroni and E. Zysman-Colman, *Asian J. Org. Chem.*, 2023, **12**, e202300347.
22 Y. Tsuchiya, S. Diesing, F. Bencheikh, Y. Wada, P. L. dos Santos, H. Kaji, E. Zysman-Colman, I. D. W. Samuel and C. Adachi, *J. Phys. Chem. A*, 2021, **25**, 8074.
23 M. Bouzrati-Zerelli, G. Noirbent, F. Goubard, T.-T. Bui, S. Villotte, C. Dietlin, F. Morlet-Savary, D. Gigmes, J. P. Fouassier, F. Dumur and J. Lalevée, *New J. Chem.*, 2018, **42**, 8261–8270.
24 S. Sem, S. Jenatsch, K. Stavrou, A. Danos, A. P. Monkman and B. Ruhstaller, *J. Mater. Chem. C*, 2022, **10**, 4878–4885.
25 X. Zhang, X. Zhao, K. Ye and J. Zhao, *Chem.–Eur. J.*, 2023, **29**, e202203737.
26 B. Limburg, *Phys. Chem. Lett.*, 2024, **15**(42), 10495–10499.
27 Y. Kwon, J. Lee, Y. Noh, D. Kim, Y. Lee, C. Yu, J. C. Roldao, S. Feng, J. Gierschner, R. Wannemacher and M. S. Kwon, *Nat. Commun.*, 2023, **14**, 92.
28 F. Garrido-Castro, H. Choubane, M. Daaou, M. C. Maestro and J. Alemán, *Chem. Commun.*, 2017, **53**, 7764–7767.

29 H. Liang, G.-Q. Xu, Z.-T. Feng, Z.-Y. Wang and P.-F. Xu, *J. Org. Chem.*, 2019, **84**(1), 60–72.
30 W.-J. Yue, C. S. Day, A. J. Brenes Rucinski and R. Martin, *Org. Lett.*, 2022, **24**(28), 5109–5114.
31 M. Montalti, A. Credi, L. Prodi and M. T. Gandolfi, *Handbook of Photochemistry*, 2006.
32 C. Wang, H. Li, T. H. Bürgin and O. S. Wenger, *Nat. Chem.*, 2024, **16**, 1151–1159.
33 F. Draper, M. L. Pattuwage, P. S. Francis, A. R. Ireland, E. G. Moore and T. U. Connell, *ACS Catal.*, 2025, **15**, 15929–15939.
34 A. Arrigo, R. Mazzaro, F. Romano, G. Bergamini and P. Ceroni, *Chem. Mater.*, 2016, **28**(18), 6664–6671.
35 H. Sun, C. Zhong and J. L. Brédas, *J. Chem. Theory Comput.*, 2015, **11**, 3851–3858.
36 K. Zhao, Ö. H. Omar, T. Nematiaram, D. Padula and A. Troisi, *J. Mater. Chem. C*, 2021, **9**, 3324–3333.
37 M. J. Goodwin, J. C. Dickenson, A. Ripak, A. M. Deetz, J. S. McCarthy, G. J. Meyer and L. Troian-Gautier, *Chem. Rev.*, 2024, **124**, 7379.
38 Y. Tamaki, K. Kamogawa, R. Inoue, P. Ceroni and O. Ishitani, *J. Am. Chem. Soc.*, 2025, **147**(36), 33010–33022.